Nanocavity Clock Spectroscopy: Resolving Competing Exciton Dynamics in WSe$_2$/MoSe$_2$ Heterobilayers

Molly A. May,[#] Tao Jiang,[#] Chenfeng Du, Kyoung-Duck Park, Xiaodong Xu, Alexey Belyanin,* and Markus B. Raschke*

Cite This: *Nano Lett.* 2021, 21, 522–528

Read Online

ACCESS | Metrics & More | Article Recommendations | SI Supporting Information

ABSTRACT: Transition-metal dichalcogenide heterostructures are an emergent platform for novel many-body states from exciton condensates to nanolasers. However, their exciton dynamics are difficult to disentangle due to multiple competing processes with time scales varying over many orders of magnitude. Using a configurable nano-optical cavity based on a plasmonic scanning probe tip, the radiative (rad) and nonradiative (nrad) relaxation of intra- and interlayer excitons is controlled. Tuning their relative rates in a WSe$_2$/MoSe$_2$ heterobilayer over 6 orders of magnitude in tip-enhanced photoluminescence spectroscopy reveals a cavity-induced crossover from nonradiative quenching to Purcell-enhanced radiation. Rate equation modeling with the interlayer charge transfer time as a reference clock allows for a comprehensive determination from the long interlayer exciton (IX) radiative lifetime $\tau_{IX}^{rad} = (94 \pm 27)$ ns to the 5 orders of magnitude faster competing nonradiative lifetime $\tau_{IX}^{nrad} = (0.6 \pm 0.2)$ ps. This approach of nanocavity clock spectroscopy is generally applicable to a wide range of excitonic systems with competing decay pathways.

KEYWORDS: *Interlayer exciton, exciton lifetime, plasmonic nanocavity, near-field spectroscopy, tip-enhanced photoluminescence*
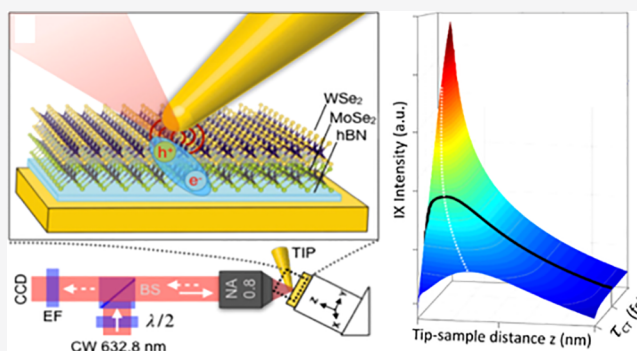
INTRODUCTION

Transition-metal dichalcogenide (TMD) heterobilayers have attracted significant attention, exhibiting novel quantum phenomena in Moiré superlattices,[1−5] correlated photon emission,[6] and valley polarized excitons.[7] Furthermore, ultrafast interlayer charge transfer in these heterobilayers can lead to the formation of interlayer excitons (IX) with long lifetimes due to their spatial separation of the electron−hole pairs.[8−16] This suggests room-temperature exciton condensation,[17] nanolasing with extended spatial coherence,[18,19] and other optoelectronic devices with atomic-scale thickness.[20−24]

However, details of their formation by ultrafast interlayer charge transfer and relaxation dynamics are difficult to access due to a convolution of several competing and coupled radiative (rad) and nonradiative (nrad) processes of the IX and the two *intra*layer excitons (X). While pump−probe and time-resolved photoluminescence (PL) have been used to measure the overall PL lifetimes of the exciton species,[11−16,25] these techniques are unable to directly discern their radiative (τ^{rad}) and nonradiative (τ^{nrad}) lifetimes. This is especially difficult for interlayer excitons with a large radiative decay rate and a weak oscillator strength.

Here, we pursue a qualitatively new approach in which we measure the PL emission from intra- and interlayer excitons while selectively Purcell enhancing τ^{rad} and modifying τ^{nrad} over several orders of magnitude using nanotip cavity interaction. This allows us to control the PL decay with a nanocavity induced crossover between excitation, nonradiative, and radiative relaxation. Using interlayer charge transver with τ_{CT} = 44 fs as a reference clock in a rate equation model for the different coupled exciton populations in steady state, we extract τ^{rad} and τ^{nrad} of the three exciton species from the different tip−sample distance-dependent evolutions of the intra- and interlayer PL intensities. With the interlayer charge transfer unaffected by the presence of the tip to first order,[8−10,26−30] we obtain obtain monolayer (ML) nonradiative lifetimes τ_X^{nrad} = (2.6 ± 0.7) ps and $\tau_{IX}^{nrad} = (0.6 \pm 0.2)$ ps, *intra*layer exciton radiative lifetime $\tau_X^{rad} = (0.7 \pm 0.2)$ ns, and an exceptionally long room-temperature IX radiative lifetime of $\tau_{IX}^{rad} = (94 \pm 27)$ ns. These results are consistent with previous measurements. They clarify that, while time-dependent photoluminescence measurements are limited by fast nonradiative decay, the IX radiative lifetime is indeed orders of magnitude longer.
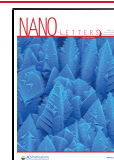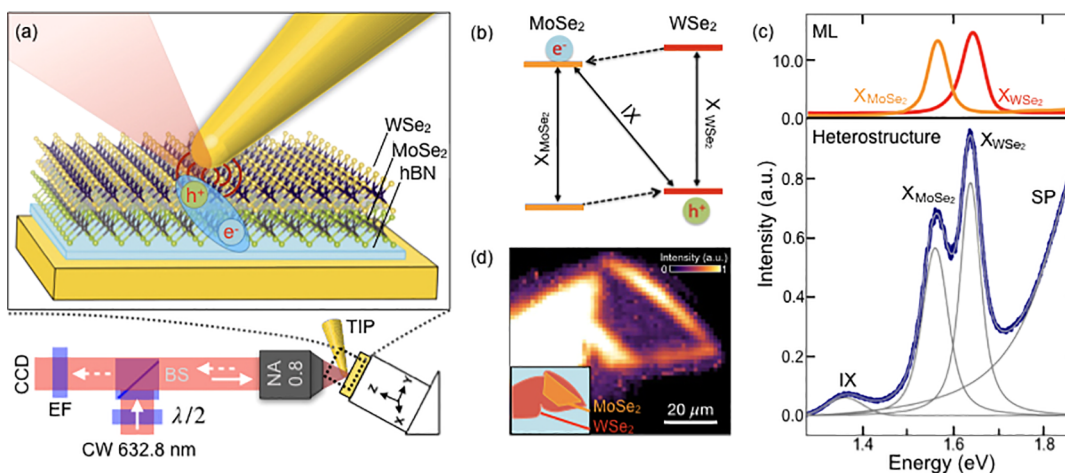
Figure 1. Tip-enhanced nanocavity clock spectroscopy. (a) Experimental setup and sample design. (b) Type II band alignment with *inter*layer exciton formation. (c) PL spectra of the TMD monolayer excitons X_{MoSe_2} (orange) and X_{WSe_2} (red) and the heterostructure (blue) with additional interlayer IX emission and localized tip plasmon PL and corresponding fits (gray). (d) Far-field micro-PL image of the sample and cartoon showing the constituent layers (inset), scale bar is 20 μm.

Additionally, the Purcell factor $F_P = 20 \pm 6$ and cavity distance-scaling exponent $n = 2.7 \pm 0.2$ of the radiative decay define field confinement, mode alignment, and scaling of the plasmonic nanocavity mode volume, which are yet poorly understood parameters in the emerging field of plasmonic nanocavity quantum electrodynamics.[31−34]

Nanocavity clock spectroscopy (NCS) thus provides a new approach to quantify the complex and competing dynamics of multiexcitonic systems complementing conventional ultrafast time-domain spectroscopy. Nanocavity control of exciton dynamics in van der Waals materials over several orders of magnitude additionally opens the door to establishing applications like high-temperature exciton condensation, tunable device fabrication, harnessing coherent emission, and control of highly localized trapping potentials such as those found in Moiré lattices.[35−39]

EXPERIMENT

Figure 1a shows the TMD heterostructure sample consisting of a WSe₂ (top) and a MoSe₂ (bottom) monolayer, separated from a template-stripped gold substrate by a hexagonal boron nitride (hBN) bilayer to reduce charge transfer between TMDs and the metal. The heterostructure is fabricated by exfoliation of the TMD monolayers and by stacking them using a polycarbonate-based dry-transfer technique with a minimal angle between their relative crystal axes.[15,40] In a home-built near-field scanning probe instrument, an electrochemically etched Au plasmonic tip and the substrate act as an optical nanocavity (see the Supporting Information for details).[41,42] The tip is tilted 35° with respect to the sample surface normal for optimal plasmonic field enhancement as shown previously[43] and positioned with a tip−sample distance accuracy of 100 pm in shear-force (SF) atomic force microscopy feedback.[44]

Tip-enhanced photoluminescence (TEPL) spectroscopy is performed in an epi-illumination and scattering geometry with continuous wave laser excitation (632.8 nm, ≤1 mW), polarized along the tip axis with a wave plate ($\lambda/2$) for polarization control, and focused onto the tip−sample junction using an 0.8 numerical aperture (NA) objective lens. The PL signal is passed through a beam splitter (BS) and a 633 nm

edge filter (EF) before detection with a grating spectrometer and charge-coupled device (CCD) camera. No tip or sample damage occurred during the measurement as assessed based on the consistent PL spectrum amplitude, shear force feedback amplitude, and exciton resonance energies over repeated tip−sample distance cycles (see Supporting Information Section I).

RESULTS

Figure 1c shows TEPL spectra of the TMD heterostructure sample (bottom) and its constituent monolayers (top). The PL signal of the heterostructure reveals three distinct peaks superimposed on top of the background surface plasmon (SP) cavity emission resonance (>1.9 eV) as shown in Figure 1c (blue) with fits to Voigt lineshapes (gray). These peaks are assigned to the WSe₂ (1.63 eV, X_{WSe_2}) and MoSe₂ (1.56 eV, X_{MoSe_2}) *intra*layer exciton emission and *inter*layer exciton emission (1.36 eV, IX), which is populated by an interlayer charge transfer in heterostructures with a type II band alignment as illustrated in Figure 1b. Figure 1d shows a micro-PL image (for the corresponding far-field spectrum, see Figure S1a) of the sample spectrally integrated between 1.3 and 1.8 eV. The heterobilayer region stands out due to its reduced PL intensity compared to the surrounding monolayer regions as expected due to the nonradiative charge transfer between the layers.[8,45]

We then perform systematic tip−sample distance dependent PL spectroscopy in the heterostructure region. The spectral response for a decreasing tip−sample distance is shown in Figure 2a from a distance of 25 nm to the point where the SF amplitude was reduced to ∼30% of its original value. From a correlation of shear force with electronic tunneling,[46] we assess that the closest distance corresponds to or very near physical atomic contact, which we define as 0 nm.

Spatio-spectral TEPL imaging of the heterostructure in this sample region shows that the emission intensity is spatially homogeneous to within 30% over a 1 μm region as shown in Figure 2b. (Note that, in some image locations, the IX response was too weak to allow for an accurate peak intensity determination, and these pixels are shown in blue.)
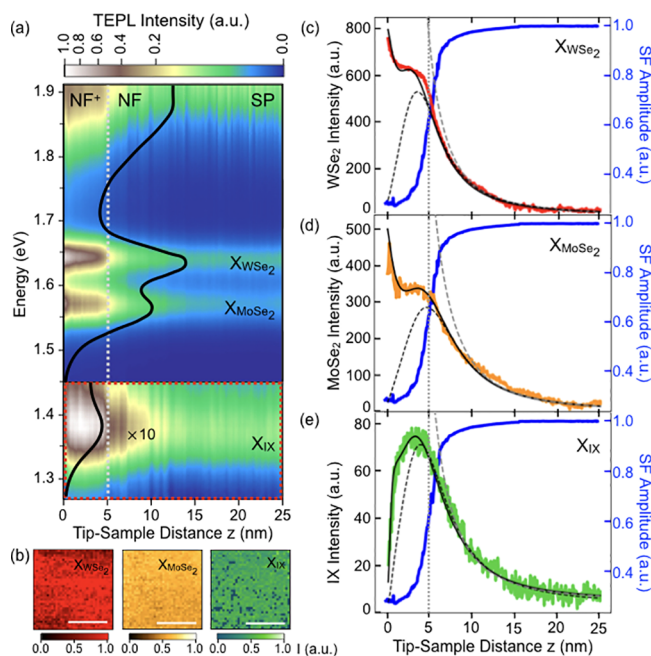
Figure 2. Tip-enhanced PL. (a) Spectral evolution of the PL signal as a function of tip−sample distance. (b) Near-field PL images (scale bar of 500 nm). (c−e) Fitted PL intensities for the WSe$_2$ (red), MoSe$_2$ (gold), and IX peaks (green), respectively, with decreasing tip−sample distance and SF feedback amplitude (blue). Also shown are fits to the data (black, solid) and simulated behavior without the effect of Purcell enhancement (black, dashed) and with near-field but no Purcell enhancement or tip-dependent nonradiative decay (gray, dashed).

Next, we plot the fitted peak intensities for the excitonic WSe$_2$ (red) and MoSe$_2$ (gold) and IX (green) emissions as a function of the tip−sample distance as shown in Figure 2c−e along with the SF amplitude (blue, right axis).

The PL spectral evolution reveals three distinct distance regimes: (i) a near-field (NF) region scaling with tip radius (~10's nm), characterized by a continuous increase of all PL peaks as established in TEPL for emitters with low quantum yields where field-enhancement dominates over PL quenching by the metallic tip.[46,47] (ii) A region of suppressed enhancement where all excitons experience increased nonradiative relaxation for 1 nm < z < 5 nm. (iii) A regime of a qualitatively distinct behavior with competing interactions driven by strongly enhanced radiative (Purcell) and nonradiative damping by the nanocavity at the closest approach (NF$^+$ region). In this region, the *intra*layer exciton signals exhibit a sharp Purcell-enhanced increase on the less than or equal to 1 nm scale, correlated with the suppression of the IX signal.

This different tip−sample distance-dependent spectral evolution in the NF and NF$^+$ regions is further highlighted from a two-dimensional (2D) covariance analysis as shown in Figure 3a,b, respectively. In the NF region (a), all peaks exhibit strong positive correlations, whereas the NF$^+$ regime (b) exhibits an anticorrelation of the IX intensity with all other PL peaks. Note that the tip plasmon PL exhibits a redshift and broadening in this region due to an increased nonradiative damping of excited carriers in this quantum-tunneling regime as observed previously.[46] The stability of the exciton PL energy indicates minimal physical disturbance to the sample by the tip which would lead to, for example, a strain-induced shift in the PL energy and possibly the formation of localized defects.[48−52]
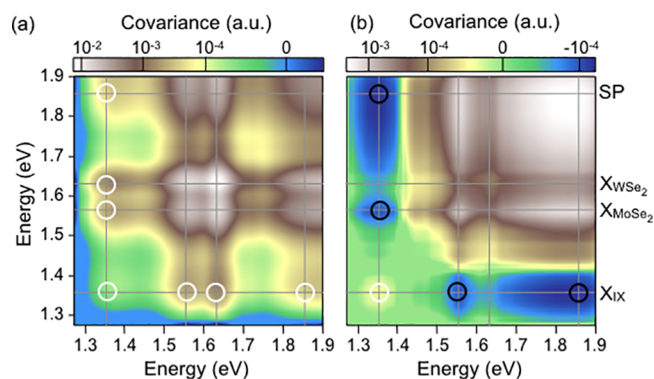

Figure 3. 2D covariance map of the PL. 2D covariance map of the PL signals in the NF region for tip−sample displacements greater than 5 nm (a) and NF$^+$ region (b) for tip−sample displacements less than 5 nm with intensity represented by a log−linear color bar.

■ MODEL

To determine the underlying X and IX time scales, we describe their distinct tip−sample distance-dependent emission as a competition between the excitation rate and the radiative and nonradiative relaxations, which are significantly modified by the tip-sample distance variation of the nanocavity coupling. For large z-values, this leads to the established tip near-field enhancement with a rise in PL intensity for both types of excitons. This effect is counteracted with decreasing distance, where a significant nonradiative relaxation via a dipole coupling to the metallic tip and substrate with subsequent ultrafast ohmic Drude damping starts to dominate, causing a turnover in the radiative emission around $z \lesssim 5$ nm. Finally, on few to sub-nanometer length scales, Purcell enhancement causes the sharp rise in the X emission. Concurrently, the IX emission is quenched, because the tip-enhanced nonradiative damping of *intra*layer excitons becomes much faster than the interlayer charge transfer.

This combined behavior can be modeled by coupled rate equations, solved analytically in the steady state to find the distance-dependent populations of each exciton species, which are used to calculate the PL intensity of each species (see the Supporting Information for details). The evolution of the *intra*layer exciton N_X and *inter*layer exciton N_{IX} populations are then given by the differences between the various excitation and relaxation rates.

$$\frac{dN_X}{dt} = F_X - (\Gamma_X^{rad} + \Gamma_X^{nrad} + \Gamma_{CT})N_X$$

$$\frac{dN_{IX}}{dt} = \Gamma_{CT}(N_M + N_W) - (\Gamma_{IX}^{rad} + \Gamma_{IX}^{nrad})N_{IX} \quad (1)$$

The excitation rate for the *intra*layer excitons F_X is then proportional to the cavity-enhanced field $F_X \propto |E/E_0|^2$, where X = M or W represents the MoSe$_2$ or WSe$_2$ *intra*layer excitons, and E_0 is the incident laser field. This near-field enhanced excitation rate scales as $F_X \propto (R/z)^m$ with R being the tip radius, z being the distance between tip and Au substrate, and m the geometry-related growth rate of the excitation and dominates over the long-range emission behavior for z > 5 nm. In contrast, the *inter*layer exciton is populated by charge transfer from the *intra*layer exciton population.

The total decay rate of each exciton species is the sum of three terms (i) Purcell-controlled radiative decay into the

cavity near-field given by $\Gamma_{X,IX}^{rad} = \Gamma_{X,IX}^{rad,0}(F_P + 1) \propto (z + d)^{-n} + \Gamma_{X,IX}^{rad,0}$, with Purcell factor F_P, minimum cavity length d, geometric scaling rate n, and free space radiative decay rate $\Gamma_{X,IX}^{rad,0}$; (ii) extrinsic tip-induced nonradiative recombination due to dipole−dipole coupling between exciton and metal[53] described by $\Gamma_{X,IX}^{nrad} \propto (R/(z + \delta z))^l$, with minimum tip-exciton separation δz and scaling exponent l; and (iii) the to first-order tip-independent intrinsic nonradiative recombination rates for each exciton $\Gamma_{X,IX}^{nrad,0}$.

While the assumptions made in this model are overall quite robust, there are some limiting cases where they break down. For example, the assumption that the excitation rate F_x is proportional to the intracavity field intensity is valid as long as the intensity is well-below saturation, as in our case. Furthermore, the interlayer exciton has in-plane and out-of-plane dipole orientation components, which both contribute to the relaxation yet with different relative weights and different tip−sample distance scaling. However, our measurements are not sensitive enough to separate these relative contributions. A detailed discussion of the limitations of our model is included in the Supporting Information, Section II.

We then fit the analytical solution to eq 1 for the TEPL intensity to the data in Figure 2c−e to globally minimize the residuals of all three exciton approach curves (black, solid lines). The resulting radiative and nonradiative exciton lifetimes for $z \to \infty$ are summarized in Table 1 along with

Table 1. Fit Parameters and Results. Fitted Model Parameters of the Intra- and Interlayer Radiative and Nonradiative Lifetimes for $z \to \infty$ and F_P for $z \to 0$

exciton lifetimes		NCS/TEPL parameters	
$\tau_{IX}^{rad,0}$	(94 ± 27) ns	F_P	(20 ± 6)
$\tau_{IX}^{nrad,0}$	(0.6 ± 0.2) ps	R	(15 ± 1) nm
$\tau_X^{rad,0}$	(0.7 ± 0.2) ns	d	(1.0 ± 0.2) nm
$\tau_X^{nrad,0}$	(2.6 ± 0.7) ps	δ_z	(0.3 ± 0.1) nm
τ_{CT}(fixed)	44 fs	n	(2.7 ± 0.2)
		l	(3.7 ± 0.1)
		m	(2.5 ± 0.1)

the other extrinsic fit parameters. Here, we assume that the tip-independent nonradiative decay of the *intra*layer excitons is dominated by ultrafast interlayer charge transfer, which was used as a reference clock with transfer time $\tau_{CT} = 2\hbar/\Gamma_{CT} = 44$ fs based on previous measurements.[8,9,10,25−30] Most existing measurements of the charge transfer time have been limited in temporal resolution by their instrument response time and thus provide only an upper limit of the true Γ_{CT}. We therefore chose a value based on the fastest temporal resolutions[8,26−29] (see the Supporting Information, Section IV). For comparison, we also performed the analysis assuming a 100 fs charge transfer time (see Table S1). All fitted parameters depend linearly on this reference time, so any uncertainty in τ_{CT} would modify the derived time constants proportionally.

To gain further insight into the interdependence and competition between exciton lifetime, Purcell enhancement, nonradiative damping, and charge transfer rate, we simulate their relative effects on the exciton emission. First, the approach behavior of the PL emission was simulated for each exciton without Purcell enhancement or nonradiative damping to the tip, as shown in Figure 2c−e (gray, dashed). This would give rise to a monotonic increase in excitation due to near-field enhancement irrespective of emitter lifetimes.

Adding the effects of nonradiative damping to the tip, but still in the absence of Purcell enhancement, the exciton emission would follow the black, dashed lines in Figure 2c−e with increased quenching due to a nonradiative charge transfer to the tip on intermediate length scales. The position and strength of this rollover in PL intensity at $z \approx 5$ nm constrains the amplitude and growth rate of the fitted τ^{nrad} term. Using these constraints from the long- and intermediate-range behaviors then allows for characterization of the short-range Purcell-enhanced PL emission. Only by going through this crossover from large z to small z are we able to retrieve the complete set of radiative and nonradiative time constants (for details see the Supporting Information).

Further, we simulate the dependence of the IX emission on, for example, charge transfer time τ_{CT} while holding the other parameters constant. As shown in Figure 4a, if the τ_{CT} is
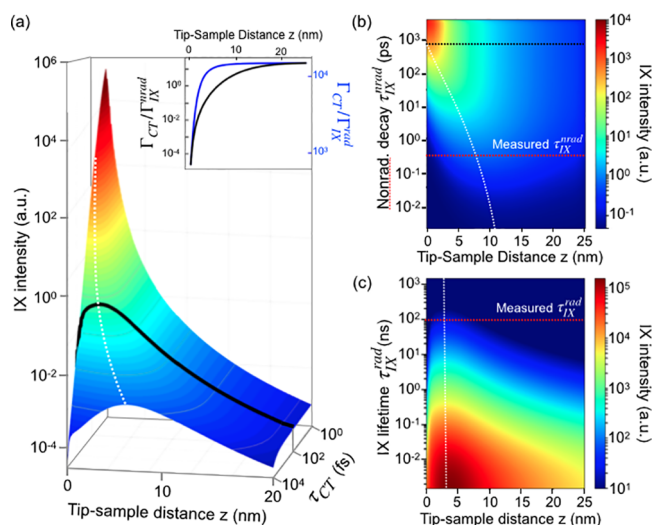

Figure 4. Simulations of IX PL dependence on τ_{CT}, τ^{nrad}, and τ_{IX}^{rad}. (a) Simulation of IX emission intensity for τ_{CT} ranging from 1 fs to 10 ps with measured data overlaid in black. (inset) Fitted values for distance-dependent rate parameters. (b) Simulation of IX emission intensity for τ_{IX}^{nrad} from 1 fs to 7 ns with measured $\tau_{IX}^{nrad} = 0.6$ ps (red, dashed line). (c) Simulation of IX emission intensity for τ_{IX}^{rad} from 1.5 ps up to 1500 ns with measured $\tau_{IX}^{rad} = 94$ ns (red, dashed line). Peak intensity evolutions (white, dashed lines) are shown for all simulations.

sufficiently fast, the IX quenching at short distances can be overcome. The inverse behavior is observed for simulated IX emission with $\tau_{CT} = 44$ fs fixed but with increasing τ^{nrad} as shown in Figure 4b. Here, the IX transitions from a short-range suppression to increasing PL intensity for sufficiently slow nonradiative decay as indicated by the black, dashed line. Finally, increasing the radiative IX lifetime leads to overall suppression of the PL signal as simulated in Figure 4c. Simulation parameters corresponding to the experimental values of τ_{IX}^{nrad} and τ_{IX}^{rad} are shown in dashed red. The distance dependence of Γ_{IX}^{nrad} and Γ_{IX}^{rad} relative to Γ_{CT} is shown in the inset of Figure 4a.

■ DISCUSSION

We now discuss the resulting fit parameters. The maximum observed nanocavity Purcell factor $F_P = (20 \pm 6)$ is consistent with the range of values of Purcell factors achieved in related plasmonic nanocavity experiments.[41,43,52,54−56] However, it is

somewhat lower than the maximum Purcell factors of $\sim 10^3$ in TEPL,[43,52,57,58] possibly due to the in-plane dipole moments of the bright TMD excitons, which are not aligned with the tip axis. Additionally, the geometric scaling parameter of the nanocavity $n = (2.7 \pm 0.2)$ indicates that the cavity mode volume scales between that of a cylinder ($n = 2$) and a sphere ($n = 3$). This result is consistent with recent finite-difference time-domain (FDTD) simulations for this cavity geometry[41] as well as calculations of the cavity volume in a quasi-normal mode framework.[42] The minimum cavity length $d = (1.0 \pm 0.2)$ nm is consistent with predictions based on the constituent ML thicknesses.[59,60] Finally, the fitted tip radius $R = (15 \pm 1)$ nm is consistent with previous investigations[46] and also with the damping of the SF amplitude starting around $z = 15$ nm, which generally occurs at tip−sample distances on the order of the tip radius.

Next, we discuss the sample properties determined by our model. The *intra*layer exciton radiative lifetime $\tau_X^{rad,0} = (0.7 \pm 0.2)$ ns at room temperature is in agreement with near nanosecond values expected from first-principles calculations,[61] which can also be inferred from the absorbance of a free-standing monolayer.[62] The IX lifetime $\tau_{IX}^{rad,0} = (94 \pm 27)$ ns is much longer than the *intra*layer lifetimes $\tau_X^{rad,0} = (0.7 \pm 0.2)$ ns, as predicted due to the spatially indirect IX transition.[63] The 2 orders of magnitude difference between *inter*layer and *intra*layer exciton radiative lifetimes agrees with what is expected based on the ratio of their respective oscillator strengths measured in ref 64, and theoretical calculations based on the optical Bloch equations predict IX lifetimes even into the microsecond range.[11] Yet, most experimental measurements of time-resolved PL in the few- to sub-nanosecond decay times[13,15,16] suggest the dominance of nonradiative decay over the observed radiative decay channels, in agreement with our results. Several investigations have observed longer IX lifetimes for valley polarized IX, by measuring at low temperature or using sample preparations that reduce nonradiative decay pathways through encapsulation with, for example, hBN,[12,14,15] but these are still limited to observing the overall PL lifetime, which is likely still dominated by nonradiative decay.

The 5 orders of magnitude faster nonradiative than radiative decay observed in this work implies a very low quantum yield of the IX. This could cause difficulty for a high-temperature exciton condensation, which requires low environmental coupling and optoelectronic devices that require high fidelity between excitation and radiative emission. However, the extremely long room-temperature IX lifetime measured here could indeed provide a platform for applications from quantum information to nanolasing, especially if the nonradiative relaxation can be suppressed.

CONCLUSION

In summary, this work demonstrates NCS as an effective new technique to quantify the dynamics of complex quantum systems with competing radiative and nonradiative excitation pathways when referenced against a known decay time constant. It is applied in TEPL to characterize, image, and control the interplay of *intra*layer and *inter*layer exciton dynamics in a $WSe_2/MoSe_2$ heterobilayer with lifetime quantification based on a rate equation model. This allows for discriminating the exceptionally long IX radiative lifetimes $\tau_{IX}^{rad,0} = (94 \pm 27)$ ns from the 5 orders of magnitude faster

nonradiative decay $\tau_{IX}^{nrad,0} = (0.6 \pm 0.2)$ ps, with the relaxation controlled by nonradiative defect scattering.

NCS can be applied to investigate the dynamics in a wide range of excitonic systems, providing a powerful complement to time-domain spectroscopy, and additionally offering nano-scale spatial resolution. For example, it could shed light on the effects of the stacking angle and charge carrier doping on the IX lifetime, isolate the highly localized IX emission in lateral heterostructures, and investigate the effects of decreasing nonradiative phonon-assisted relaxation or shifts in emission energy in low-temperature experiments. It could be adapted for a broad range of applications from providing a mechanism for switching the emission of localized single-photon emitting defects such as those found in WSe_2, hBN, or diamond[65−67] to increasing exciton densities to enable new optoelectronic applications or to induce room-temperature exciton condensates[23,68,69] or superfluidity.[68,70]

■ ASSOCIATED CONTENT

ⓢ Supporting Information

The Supporting Information is available free of charge at https://pubs.acs.org/doi/10.1021/acs.nanolett.0c03979.

> Details of the experiment and sample characterization; details of the theoretical model and its limiting cases; and details of the selection and effect of the charge transfer time (PDF)

■ AUTHOR INFORMATION

Corresponding Authors

Alexey Belyanin − *Department of Physics and Astronomy, Texas A&M University, College Station 77843, Texas, United States*; Email: belyanin@tamu.edu

Markus B. Raschke − *Department of Physics, Department of Chemistry, and JILA, University of Colorado, Boulder 80309, Colorado, United States*; ⓞ orcid.org/0000-0003-2822-851X; Email: markus.raschke@colorado.edu

Authors

Molly A. May − *Department of Physics, Department of Chemistry, and JILA, University of Colorado, Boulder 80309, Colorado, United States*; ⓞ orcid.org/0000-0001-7164-9569

Tao Jiang − *MOE Key Laboratory of Advanced Micro-Structured Materials, and School of Physics Science and Engineering, Tongji University, Shanghai 200092, China; Department of Physics, Department of Chemistry, and JILA, University of Colorado, Boulder 80309, Colorado, United States*; ⓞ orcid.org/0000-0001-8656-1738

Chenfeng Du − *Department of Physics, University of Washington, Seattle 98195, Washington, United States*

Kyoung-Duck Park − *Department of Physics, School of Natural Sciences, Ulsan National Institute of Science and Technology, Ulsan, South Korea; Department of Physics, Department of Chemistry, and JILA, University of Colorado, Boulder 80309, Colorado, United States*; ⓞ orcid.org/0000-0002-9302-9384

Xiaodong Xu − *Department of Physics, University of Washington, Seattle 98195, Washington, United States*

Complete contact information is available at:
https://pubs.acs.org/10.1021/acs.nanolett.0c03979

■ REFERENCES

(1) Tran, K.; et al. Evidence for moiré excitons in van der Waals heterostructures. *Nature* **2019**, *567*, 71−75.

(2) Alexeev, E. M.; et al. Resonantly hybridized excitons in moiré superlattices in van der Waals heterostructures. *Nature* **2019**, *567*, 81−86.

(3) Seyler, K. L.; Rivera, P.; Yu, H.; Wilson, N. P.; Ray, E. L.; Mandrus, D. G.; Yan, J.; Yao, W.; Xu, X. Signatures of moire-trapped valley excitons in MoSe2/WSe2 heterobilayers. *Nature* **2019**, *567*, 66−70.

(4) Jin, C.; Regan, E. C.; Yan, A.; Iqbal Bakti Utama, M.; Wang, D.; Zhao, S.; Qin, Y.; Yang, S.; Zheng, Z.; Shi, S.; Watanabe, K.; Taniguchi, T.; Tongay, S.; Zettl, A.; Wang, F. Observation of moire excitons in WSe2/WS2 heterostructure superlattices. *Nature* **2019**, *567*, 76−80.

(5) Kunstmann, J.; Mooshammer, F.; Nagler, P.; Chaves, A.; Stein, F.; Paradiso, N.; Plechinger, G.; Strunk, C.; Schüller, C.; Seifert, G.; Reichman, D. R.; Korn, T. Momentum-space indirect interlayer excitons in transition-metal dichalcogenide van der Waals heterostructures. *Nat. Phys.* **2018**, *14*, 801−805.

(6) Xu, W.; Liu, W.; Schmidt, J. F.; Zhao, W.; Lu, X.; Raab, T.; Diederichs, C.; Gao, W.; Seletskiy, D. V.; Xiong, Q. Correlated fluorescence blinking in two-dimensional semiconductor heterostructures. *Nature* **2017**, *541*, 62−67.

(7) Rivera, P.; Seyler, K. L.; Yu, H.; Schaibley, J. R.; Yan, J.; Mandrus, D. G.; Yao, W.; Xu, X. Valley-polarized exciton dynamics in a 2D semiconductor heterostructure. *Science* **2016**, *351*, 688−691.

(8) Chen, H.; Wen, X.; Zhang, J.; Wu, T.; Gong, Y.; Zhang, X.; Yuan, J.; Yi, C.; Lou, J.; Ajayan, P. M.; Zhuang, W.; Zhang, G.; Zheng, J. Ultrafast formation of interlayer hot excitons in atomically thin MoS2/WS2 heterostructures. *Nat. Commun.* **2016**, *7*, 12512.

(9) Ji, Z.; Hong, H.; Zhang, J.; Zhang, Q.; Huang, W.; Cao, T.; Qiao, R.; Liu, C.; Liang, J.; Jin, C.; Jiao, L.; Shi, K.; Meng, S.; Liu, K. Robust Stacking-Independent Ultrafast Charge Transfer in MoS$_2$/WS$_2$ Bilayers. *ACS Nano* **2017**, *11*, 12020−12026.

(10) Zheng, Q.; Saidi, W. A.; Xie, Y.; Lan, Z.; Prezhdo, O. V.; Petek, H.; Zhao, J. Phonon-Assisted Ultrafast Charge Transfer at van der Waals Heterostructure Interface. *Nano Lett.* **2017**, *17*, 6435−6442.

(11) Ovesen, S.; Brem, S.; Linderälv, C.; Kuisma, M.; Korn, T.; Erhart, P.; Selig, M.; Malic, E. Interlayer exciton dynamics in van der Waals heterostructures. *Communications Physics* **2019**, *2*, 23.

(12) Okada, M.; Kutana, A.; Kureishi, Y.; Kobayashi, Y.; Saito, Y.; Saito, T.; Watanabe, K.; Taniguchi, T.; Gupta, S.; Miyata, Y.; Yakobson, B. I.; Shinohara, H.; Kitaura, R. Direct and Indirect Interlayer Excitons in a van der Waals Heterostructure of hBN/WS$_2$/MoS$_2$/hBN. *ACS Nano* **2018**, *12*, 2498−2505.

(13) Nagler, P.; Plechinger, G.; Ballottin, M. V.; Mitioglu, A.; Meier, S.; Paradiso, N.; Strunk, C.; Chernikov, A.; Christianen, P. C. M.;

Schüller, C.; Korn, T. Interlayer exciton dynamics in a dichalcogenide monolayer heterostructure. *2D Mater.* **2017**, *4*, No. 025112.

(14) Miller, B.; Steinhoff, A.; Pano, B.; Klein, J.; Jahnke, F.; Holleitner, A.; Wurstbauer, U. Long-Lived Direct and Indirect Interlayer Excitons in van der Waals Heterostructures. *Nano Lett.* **2017**, *17*, 5229−5237.

(15) Rivera, P.; Schaibley, J. R.; Jones, A. M.; Ross, J. S.; Wu, S.; Aivazian, G.; Klement, P.; Seyler, K.; Clark, G.; Ghimire, N. J.; Yan, J.; Mandrus, D. G.; Yao, W.; Xu, X. Observation of long-lived interlayer excitons in monolayer MoSe2−WSe2 heterostructures. *Nat. Commun.* **2015**, *6*, 6242.

(16) Baranowski, M.; Surrente, A.; Klopotowski, L.; Urban, J. M.; Zhang, N.; Maude, D. K.; Wiwatowski, K.; Mackowski, S.; Kung, Y. C.; Dumcenco, D.; Kis, A.; Plochocka, P. Probing the Interlayer Exciton Physics in a MoS$_2$/MoSe$_2$/MoS$_2$ van der Waals Heterostructure. *Nano Lett.* **2017**, *17*, 6360−6365.

(17) Levi, B. G. A Dark-Horse Entry in the Race for an Excitonic Condensate. *Phys. Today* **2004**, *57*, 21−23.

(18) Muller, E. A.; Pollard, B.; Bechtel, H. A.; Adato, R.; Etezadi, D.; Altug, H.; Raschke, M. B. Nanoimaging and control of molecular vibrations through electromagnetically induced scattering reaching the strong coupling regime. *ACS Photonics* **2018**, *5*, 3594−3600.

(19) Paik, E. Y.; Zhang, L.; Burg, G. W.; Gogna, R.; Tutuc, E.; Deng, H. Interlayer exciton laser of extended spatial coherence in atomically thin heterostructures. *Nature* **2019**, *576*, 80−84.

(20) Liu, Y.; Weiss, N. O.; Duan, X.; Cheng, H.-C.; Huang, Y.; Duan, X. Van der Waals heterostructures and devices. *Nat. Rev. Mater.* **2016**, *1*, 16042.

(21) Iannaccone, G.; Bonaccorso, F.; Colombo, L.; Fiori, G. Quantum engineering of transistors based on 2D materials heterostructures. *Nat. Nanotechnol.* **2018**, *13*, 183−191.

(22) Massicotte, M.; Schmidt, P.; Vialla, F.; Schädler, K. G.; Reserbat-Plantey, A.; Watanabe, K.; Taniguchi, T.; Tielrooij, K. J.; Koppens, F. H. L. Picosecond photoresponse in van der Waals heterostructures. *Nat. Nanotechnol.* **2016**, *11*, 42−46.

(23) Wong, J.; Jariwala, D.; Tagliabue, G.; Tat, K.; Davoyan, A. R.; Sherrott, M. C.; Atwater, H. A. High Photovoltaic Quantum Efficiency in Ultrathin van der Waals Heterostructures. *ACS Nano* **2017**, *11*, 7230−7240.

(24) Ross, J. S.; Rivera, P.; Schaibley, J.; Lee-Wong, E.; Yu, H.; Taniguchi, T.; Watanabe, K.; Yan, J.; Mandrus, D.; Cobden, D.; Yao, W.; Xu, X. Interlayer Exciton Optoelectronics in a 2D Heterostructure p−n Junction. *Nano Lett.* **2017**, *17*, 638−643.

(25) Peng, B.; Yu, G.; Liu, X.; Liu, B.; Liang, X.; Bi, L.; Deng, L.; Sum, T. C.; Loh, K. P. Ultrafast charge transfer in MoS$_2$/WSe$_2$ pn Heterojunction. *2D Mater.* **2016**, *3*, No. 025020.

(26) Rigosi, A. F.; Hill, H. M.; Li, Y.; Chernikov, A.; Heinz, T. F. Probing Interlayer Interactions in Transition Metal Dichalcogenide Heterostructures by Optical Spectroscopy: MoS$_2$/WS$_2$ and MoSe$_2$/WSe$_2$. *Nano Lett.* **2015**, *15*, 5033−5038.

(27) Hong, X.; Kim, J.; Shi, S.-F.; Zhang, Y.; Jin, C.; Sun, Y.; Tongay, S.; Wu, J.; Zhang, Y.; Wang, F. Ultrafast charge transfer in atomically thin MoS2/WS2 heterostructures. *Nat. Nanotechnol.* **2014**, *9*, 682−686.

(28) Zheng, Q.; Xie, Y.; Lan, Z.; Prezhdo, O. V.; Saidi, W. A.; Zhao, J. Phonon-coupled ultrafast interlayer charge oscillation at van der Waals heterostructure interfaces. *Phys. Rev. B: Condens. Matter Mater. Phys.* **2018**, *97*, 205417.

(29) Zhu, H.; Wang, J.; Gong, Z.; Kim, Y. D.; Hone, J.; Zhu, X.-Y. Interfacial Charge Transfer Circumventing Momentum Mismatch at Two-Dimensional van der Waals Heterojunctions. *Nano Lett.* **2017**, *17*, 3591−3598.

(30) Ceballos, F.; Bellus, M. Z.; Chiu, H.-Y.; Zhao, H. Ultrafast Charge Separation and Indirect Exciton Formation in a MoS$_2$−MoSe$_2$ van der Waals Heterostructure. *ACS Nano* **2014**, *8*, 12717−12724.

(31) Waldron, R. Perturbation theory of resonant cavities. *Proc. Inst. Electr. Eng., Part C* **1960**, *107*, 272.

(32) Maier, S. A. Effective Mode Volume of Nanoscale Plasmon Cavities. *Opt. Quantum Electron.* **2006**, *38*, 257−267.

(33) Kristensen, P. T.; Hughes, S. Modes and Mode Volumes of Leaky Optical Cavities and Plasmonic Nanoresonators. *ACS Photonics* **2014**, *1*, 2−10.

(34) Cognée, K. G.; Yan, W.; La China, F.; Balestri, D.; Intonti, F.; Gurioli, M.; Koenderink, A. F.; Lalanne, P. Mapping complex mode volumes with cavity perturbation theory. *Optica* **2019**, *6*, 269.

(35) Mak, K. F.; Shan, J. Opportunities and challenges of interlayer exciton control and manipulation. *Nat. Nanotechnol.* **2018**, *13*, 974−976.

(36) Jin, C.; Ma, E. Y.; Karni, O.; Regan, E. C.; Wang, F.; Heinz, T. F. Ultrafast dynamics in van der Waals heterostructures. *Nat. Nanotechnol.* **2018**, *13*, 994−1003.

(37) Ovesen, S.; Brem, S.; Linderälv, C.; Kuisma, M.; Korn, T.; Erhart, P.; Selig, M.; Malic, E. Interlayer exciton dynamics in van der Waals heterostructures. *Communications Physics* **2019**, *2*, 1−8.

(38) Tartakovskii, A. Excitons in 2D heterostructures. *Nature Reviews Physics* **2020**, *2*, 8−9.

(39) Xie, K.; Li, X.; Cao, T. Theory and Ab Initio Calculation of Optically Excited States—Recent Advances in 2D Materials. *Adv. Mater.* **2019**, 1904306.

(40) Zomer, P. J.; Guimaraes, M. H. D.; Brant, J. C.; Tombros, N.; van Wees, B. J. Fast pick up technique for high quality heterostructures of bilayer graphene and hexagonal boron nitride. *Appl. Phys. Lett.* **2014**, *105*, No. 013101.

(41) Park, K.-D.; May, M. A.; Leng, H.; Wang, J.; Kropp, J. A.; Gougousi, T.; Pelton, M.; Raschke, M. B. Tip-enhanced strong coupling spectroscopy, imaging, and control of a single quantum emitter. *Science advances* **2019**, *5*, No. eaav5931.

(42) May, M. A.; Fialkow, D.; Wu, T.; Park, K.; Leng, H.; Kropp, J. A.; Gougousi, T.; Lalanne, P.; Pelton, M.; Raschke, M. B. Nano-Cavity QED with Tunable Nano-Tip Interaction. *Advanced Quantum Technologies* **2020**, *3*, 1900087.

(43) Park, K.-D.; Raschke, M. B. Polarization Control with Plasmonic Antenna Tips: A Universal Approach to Optical Nano-crystallography and Vector-Field Imaging. *Nano Lett.* **2018**, *18*, 2912−2917.

(44) Raschke, M. B.; Lienau, C. Apertureless near-field optical microscopy: Tip−sample coupling in elastic light scattering. *Appl. Phys. Lett.* **2003**, *83*, 5089−5091.

(45) Tongay, S.; Fan, W.; Kang, J.; Park, J.; Koldemir, U.; Suh, J.; Narang, D. S.; Liu, K.; Ji, J.; Li, J.; Sinclair, R.; Wu, J. Tuning Interlayer Coupling in Large-Area Heterostructures with CVD-Grown MoS₂ and WS₂ Monolayers. *Nano Lett.* **2014**, *14*, 3185−3190.

(46) Kravtsov, V.; Berweger, S.; Atkin, J. M.; Raschke, M. B. Control of Plasmon Emission and Dynamics at the Transition from Classical to Quantum Coupling. *Nano Lett.* **2014**, *14*, 5270−5275.

(47) Anger, P.; Bharadwaj, P.; Novotny, L. Enhancement and Quenching of Single-Molecule Fluorescence. *Phys. Rev. Lett.* **2006**, *96*, 113002.

(48) Conley, H. J.; Wang, B.; Ziegler, J. I.; Haglund, R. F.; Pantelides, S. T.; Bolotin, K. I. Bandgap Engineering of Strained Monolayer and Bilayer MoS₂. *Nano Lett.* **2013**, *13*, 3626−3630.

(49) Kumar, S.; Kaczmarczyk, A.; Gerardot, B. D. Strain-Induced Spatial and Spectral Isolation of Quantum Emitters in Mono- and Bilayer WSe₂. *Nano Lett.* **2015**, *15*, 7567−7573.

(50) Sarwat, S. G.; Tweedie, M.; Porter, B. F.; Zhou, Y.; Sheng, Y.; Mol, J.; Warner, J.; Bhaskaran, H. Revealing strain-induced effects in ultrathin heterostructures at the nanoscale. *Nano Lett.* **2018**, *18*, 2467−2474.

(51) Aslan, O. B.; Deng, M.; Heinz, T. F. Strain tuning of excitons in monolayer WSe₂. *Phys. Rev. B: Condens. Matter Mater. Phys.* **2018**, *98*, 115308.

(52) Park, K.-D.; Khatib, O.; Kravtsov, V.; Clark, G.; Xu, X.; Raschke, M. B. Hybrid tip-enhanced nanospectroscopy and nano-imaging of monolayer WSe₂ with local strain control. *Nano Lett.* **2016**, *16*, 2621−2627.

(53) Forster, T. Intermolecular Energy Migration and Fluorescence. *Annals Phys.* **1948**, *2*, 55−75.

(54) Srinivasan, V.; Ramamurthy, S. S. Purcell Factor: A Tunable Metric for Plasmon-Coupled Fluorescence Emission Enhancements in Cermet Nanocavities. *J. Phys. Chem. C* **2016**, *120*, 2908−2913.

(55) Akselrod, G. M.; Argyropoulos, C.; Hoang, T. B.; Ciraci, C.; Fang, C.; Huang, J.; Smith, D. R.; Mikkelsen, M. H. Probing the mechanisms of large Purcell enhancement in plasmonic nano-antennas. *Nat. Photonics* **2014**, *8*, 835−840.

(56) Kongsuwan, N.; Demetriadou, A.; Chikkaraddy, R.; Benz, F.; Turek, V. A.; Keyser, U. F.; Baumberg, J. J.; Hess, O. Suppressed Quenching and Strong-Coupling of Purcell-Enhanced Single-Molecule Emission in Plasmonic Nanocavities. *ACS Photonics* **2018**, *5*, 186−191.

(57) Wei, W.; Yan, X.; Zhang, X. Ultrahigh Purcell factor in low-threshold nanolaser based on asymmetric hybrid plasmonic cavity. *Sci. Rep.* **2016**, *6*, 33063.

(58) Suh, J. Y.; Kim, C. H.; Zhou, W.; Huntington, M. D.; Co, D. T.; Wasielewski, M. R.; Odom, T. W. Plasmonic Bowtie Nanolaser Arrays. *Nano Lett.* **2012**, *12*, 5769−5774.

(59) Xu, K.; Wang, Z.; Du, X.; Safdar, M.; Jiang, C.; He, J. Atomic-layer triangular WSe₂ sheets: synthesis and layer-dependent photoluminescence property. *Nanotechnology* **2013**, *24*, 465705.

(60) Li, X.; Zhu, H. Two-dimensional MoS2: Properties, preparation, and applications. *Journal of Materiomics* **2015**, *1*, 33−44.

(61) Palummo, M.; Bernardi, M.; Grossman, J. C. Exciton Radiative Lifetimes in Two-Dimensional Transition Metal Dichalcogenides. *Nano Lett.* **2015**, *15*, 2794−2800.

(62) Jin, C.; Kim, J.; Wu, K.; Chen, B.; Barnard, E. S.; Suh, J.; Shi, Z.; Drapcho, S. G.; Wu, J.; Schuck, P. J.; et al. On optical dipole moment and radiative recombination lifetime of excitons in WSe2. *Adv. Funct. Mater.* **2017**, *27*, 1601741.

(63) Novoselov, K. S.; Mishchenko, A.; Carvalho, A.; Castro Neto, A. H. 2D materials and van der Waals heterostructures. *Science* **2016**, *353*, aac9439.

(64) Ross, J. S.; Rivera, P.; Schaibley, J.; Lee-Wong, E.; Yu, H.; Taniguchi, T.; Watanabe, K.; Yan, J.; Mandrus, D.; Cobden, D.; et al. Interlayer exciton optoelectronics in a 2D heterostructure p−n junction. *Nano Lett.* **2017**, *17*, 638−643.

(65) Koperski, M.; Nogajewski, K.; Arora, A.; Cherkez, V.; Mallet, P.; Veuillen, J.-Y.; Marcus, J.; Kossacki, P.; Potemski, M. Single photon emitters in exfoliated WSe2 structures. *Nat. Nanotechnol.* **2015**, *10*, 503−506.

(66) Grosso, G.; Moon, H.; Lienhard, B.; Ali, S.; Efetov, D. K.; Furchi, M. M.; Jarillo-Herrero, P.; Ford, M. J.; Aharonovich, I.; Englund, D. Tunable and high-purity room temperature single-photon emission from atomic defects in hexagonal boron nitride. *Nat. Commun.* **2017**, *8*, 1−8.

(67) Beveratos, A.; Kühn, S.; Brouri, R.; Gacoin, T.; Poizat, J.-P.; Grangier, P. Room temperature stable single-photon source. *European Physical Journal D-Atomic, Molecular, Optical and Plasma Physics* **2002**, *18*, 191−196.

(68) Su, J.-J.; MacDonald, A. H. How to make a bilayer exciton condensate flow. *Nat. Phys.* **2008**, *4*, 799−802.

(69) Mak, K. F.; Shan, J. Opportunities and challenges of interlayer exciton control and manipulation. *Nat. Nanotechnol.* **2018**, *13*, 974−976.

(70) Fogler, M. M.; Butov, L. V.; Novoselov, K. S. High-temperature superfluidity with indirect excitons in van der Waals heterostructures. *Nat. Commun.* **2014**, *5*, 4555.